Structure-Based Virtual Screening and Molecular Dynamics Investigation of Natural Bioactive Compounds Against SARS-CoV-2 Proteins

Yoshua B. Mtulo , Angelina I. Makaye , Fidele Ntie-Kang * , Lucas Paul *

Posted Date: 4 June 2026

doi: 10.20944/preprints202606.0440.v1

Keywords: SARS-CoV-2; amentoflavone; molecular docking; MD simulation; free energy landscape analysis

 doi:10.20944/preprints202606.0440.v1

Article

Structure-Based Virtual Screening and Molecular Dynamics Investigation of Natural Bioactive Compounds Against SARS-CoV-2 Proteins

Yoshua B. Mtulo [1], Angelina I. Makaye [2], Fidele Ntie-Kang [3,4,5,*] and Lucas Paul [6,*]

[1] Department of Educational Psychology and Curriculum Studies, College of Education, University of Dodoma, Dodoma, Tanzania
[2] Department of Chemistry, College of Natural and Mathematical Sciences, University of Dodoma, Dodoma, Tanzania
[3] Center for Drug Discovery, University of Buea, Buea, Cameroon
[4] Department of Chemistry, University of Buea, Buea, Cameroon
[5] Institute of Pharmacy, Martin-Luther University Halle-Wittenberg, Halle (Saale), Germany
[6] Department of Chemistry, Dar es Salaam University College of Education, University of Dar es Salaam, Dar es Salaam, Tanzania
* Correspondence: fidele.ntie-kang@ubuea.cm (F.N.-K.); lucaspaul33@gmail.com (L.P.)

Abstract

The continuous emergence of SARS-CoV-2 variants necessitates the identification of effective multi-target antiviral agents with enhanced stability and binding efficiency. This study employed an integrated computational approach, including molecular docking, molecular dynamics (MD) simulations, free energy landscape (FEL) analysis, and Molecular Mechanics Poisson-Boltzmann Surface Area (MM-PBSA) calculations, to evaluate the inhibitory potential of twenty natural compounds against SARS-CoV-2 proteins 7XJW, 8DRW, and 9PFH. Molecular docking identified Amentoflavone as the most promising candidate, exhibiting strong binding affinities toward all targets through favorable hydrogen-bond and hydrophobic interactions within the active sites. Interaction analysis revealed that its biflavonoid scaffold promoted extensive ligand–protein complementarity through hydroxyl and aromatic functional groups. MD simulations demonstrated stable protein-ligand complexes, characterized by low fluctuations in RMSD, RMSF, SASA, and radius of gyration values throughout the 100 ns trajectories. Persistent hydrogen-bond interactions further supported complex stability. FEL analysis revealed compact low-energy conformational basins, indicating thermodynamically favorable binding states. MM-PBSA calculations confirmed favorable binding free energies primarily driven by van der Waals and electrostatic contributions, with the 7XJW-Amentoflavone complex exhibiting the most favorable energetic profile. Overall, these findings highlight Amentoflavone as a promising multi-target inhibitor and potential lead compound for future antiviral drug development and experimental validation against SARS-CoV-2.

Keywords: SARS-CoV-2; amentoflavone; molecular docking; MD simulation; free energy landscape analysis

1. Introduction

Coronavirus disease 2019 (COVID-19), caused by the novel severe acute respiratory syndrome coronavirus 2 (SARS-CoV-2), emerged in late 2019 and rapidly evolved into one of the most devastating global public health emergencies of the 21st century. SARS-CoV-2 belongs to the β-coronavirus genus and is characterized as an enveloped, positive-sense single-stranded RNA virus [1,2]. Previous coronavirus outbreaks, including severe acute respiratory syndrome coronavirus (SARS-CoV) in 2003 and Middle East respiratory syndrome coronavirus (MERS-CoV) in 2012,

 doi:10.20944/preprints202606.0440.v1

demonstrated the pandemic potential of coronaviruses [3–5]. However, the unprecedented transmissibility and global spread of SARS-CoV-2 resulted in extensive morbidity, mortality, and socioeconomic disruption worldwide [6]. Clinically, COVID-19 presents with a broad spectrum of manifestations ranging from asymptomatic infection and mild respiratory symptoms to severe pneumonia, acute respiratory distress syndrome (ARDS), multi-organ dysfunction, and death, particularly among elderly individuals and patients with underlying comorbidities [7].

The impact of the pandemic varied considerably across geographical regions due to differences in healthcare infrastructure, socioeconomic conditions, public health preparedness, and access to therapeutics and vaccines. Although high-income countries initially reported the highest numbers of infections and fatalities, low- and middle-income regions, including many African countries, later experienced substantial health and economic burdens [8,9]. In Africa, limited diagnostic capacity, inadequate intensive care facilities, and unequal vaccine distribution contributed to challenges in disease management [10,11]. Despite mortality rates being lower than initially predicted, the pandemic significantly strained fragile healthcare systems and disrupted essential health services, including the management of malaria, tuberculosis, and HIV/AIDS. Furthermore, the socioeconomic consequences of prolonged lockdowns and healthcare disruptions highlighted the urgent need for affordable, accessible, and effective therapeutic interventions suitable for resource-limited settings [12].

Current management strategies for COVID-19 primarily rely on supportive care, vaccination programs, and antiviral therapeutics [13,14]. Several drugs, including remdesivir, dexamethasone, anticoagulants, and combinations such as nirmatrelvir/ritonavir (Paxlovid), have been employed to reduce disease severity and viral replication [15–17]. Although these therapeutic agents have demonstrated varying degrees of clinical benefit, important limitations remain, including reduced efficacy against emerging viral variants, adverse effects, high treatment costs, and unequal global accessibility [18]. In addition, the continuous emergence of SARS-CoV-2 variants raises concerns regarding drug resistance and the long-term effectiveness of currently available therapies [1,2]. These challenges emphasize the necessity for continuous drug discovery efforts targeting essential viral proteins involved in replication, transcription, and host-cell entry, such as the main protease (3CLpro), papain-like protease (PLpro), RNA-dependent RNA polymerase (RdRp), helicase, and spike glycoprotein.

Natural products have emerged as valuable sources of antiviral compounds due to their remarkable structural diversity, broad biological activities, and generally favorable safety profiles [19]. Numerous phytochemicals, particularly flavonoids, terpenoids, quinones, and alkaloids, have demonstrated inhibitory potential against SARS-CoV-2 proteins in both computational and experimental investigations [20]. Also, compounds such as curcumin, quercetin, luteolin, apigenin, celastrol, tannic acid, and cryptotanshinone have shown promising binding interactions with viral enzymes responsible for replication and proteolytic processing [21]. In addition to direct antiviral effects, many natural compounds possess anti-inflammatory and immunomodulatory properties that may contribute to the mitigation of COVID-19-associated complications [22,23]. Nevertheless, several of these bioactive molecules exhibit pharmacokinetic limitations, including poor solubility, low bioavailability, and rapid metabolism, necessitating systematic computational screening to identify candidates with optimal drug-like characteristics and therapeutic potential [22].

In the present study, a comprehensive computational approach was employed to evaluate selected natural bioactive compounds against key SARS-CoV-2 target proteins. Protein structures with accession codes 7XJW, 8DRW, and 9PFH, retrieved from the Protein Data Bank (PDB) [24], were selected to represent critical viral proteins involved in replication and host interaction. A diverse library of natural compounds (Figure 1), including Pristimerin, Hesperetin, Diplacone, Luteolin, Bavachinin, Betulinic acid, Curcumin, Rosmariquinone, Psoralidin, Cryptotanshinone, Iguesterin, Hirsutenone, Tingenone, Apigenin, Amentoflavone, Mimulone, Celastrol, Quercetin, Methyl tanshinonate, and Savinin, was subjected to virtual screening and molecular docking analyses to predict binding affinities and interaction profiles with the selected viral targets. The most promising ligand-protein complexes were subsequently investigated using molecular dynamics (MD) simulations to evaluate their conformational stability, structural flexibility, and interaction

 doi:10.20944/preprints202606.0440.v1

persistence under dynamic physiological conditions. Furthermore, binding free energy calculations were performed to estimate the thermodynamic favorability of ligand binding and to identify potential lead compounds for further development.

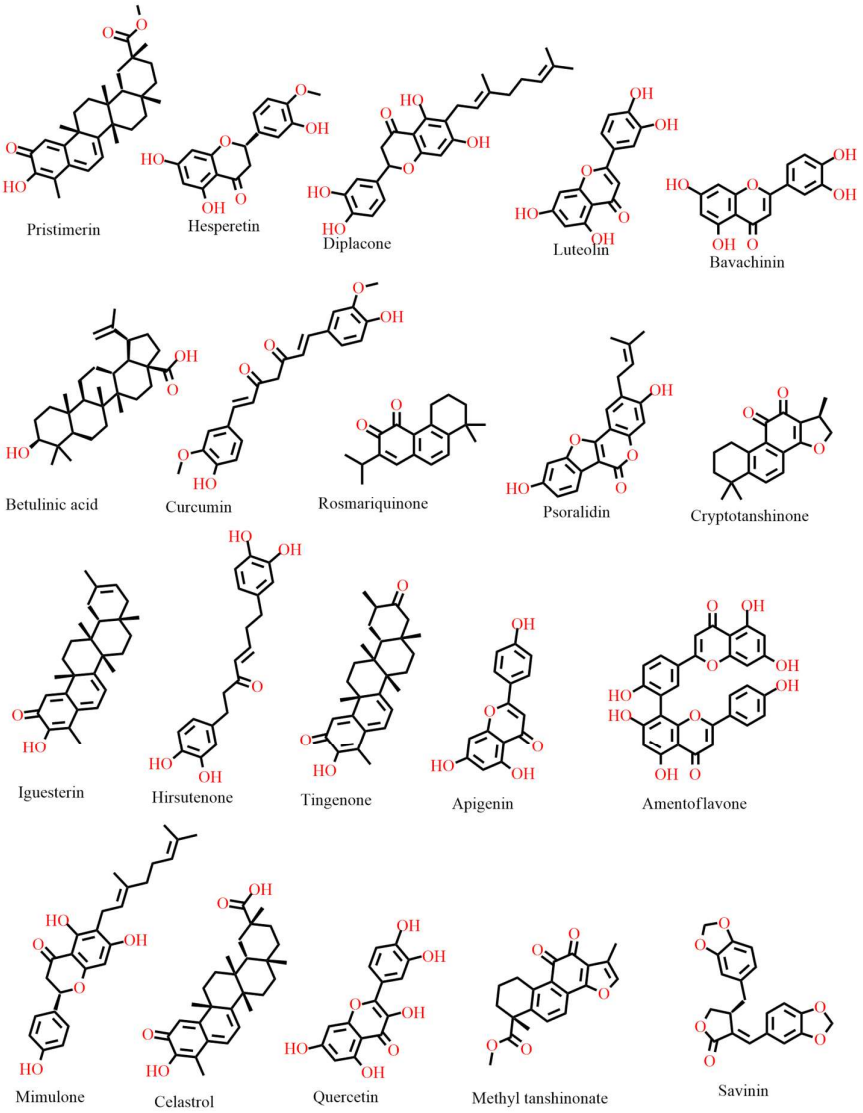

Figure 1. Chemical structures of representative natural compounds investigated as potential SARS-CoV-2 inhibitors, highlighting the structural diversity and pharmacophoric features associated with antiviral activity and therapeutic potential against COVID-19.

The primary objective of this study is to identify potential natural inhibitors of SARS-CoV-2 proteins through an integrated computational workflow involving molecular docking, molecular dynamics simulations, free energy landscape calculations, and Molecular Mechanics Poisson-Boltzmann Surface Area (MM-PBSA) analysis. Specifically, the study aims to determine the binding affinities of selected natural compounds toward essential viral targets and evaluate the stability, conformational behavior, and persistence of protein-ligand interactions under dynamic physiological conditions. The findings of this study may contribute to the identification of promising multi-target antiviral agents derived from natural products and provide valuable insights for future experimental validation and therapeutic development. Furthermore, by integrating multiple computational approaches, this work offers a cost-effective and time-efficient strategy for accelerating the discovery of novel antiviral candidates against emerging and re-emerging viral pathogens.

 doi:10.20944/preprints202606.0440.v1

2. Methods

2.1. Ligand and Protein Preparation

The chemical structures of the selected natural compounds, including Pristimerin, Hesperetin, Diplacone, Luteolin, Bavachinin, Betulinic acid, Curcumin, Rosmariquinone, Psoralidin, Cryptotanshinone, Iguesterin, Hirsutenone, Tingenone, Apigenin, Amentoflavone, Mimulone, Celastrol, Quercetin, Methyl tanshinonate, and Savinin, were retrieved from Pubchem data base [25]. Ligand structures were converted into Protein Data Bank (PDB) format using OpenBabel [26], followed by geometry optimization and generation of ligand topologies and force field parameters using LigParGen [27]. The generated parameters included bond, angle, dihedral, Lennard-Jones [28], and partial atomic charge information required for molecular docking and molecular dynamics simulations.

The three-dimensional crystal structures of the SARS-CoV-2 target proteins 7XJW [29], 8DRW [30], and 9PFH [29] were retrieved from the Protein Data Bank (PDB) [24,31]. Prior to computational analysis, the proteins were prepared by removing co-crystallized ligands, water molecules, and unnecessary heteroatoms to avoid interference with ligand binding using UCSF Chimera [32,33]. Missing hydrogen atoms were added, and appropriate protonation states and partial charges were assigned to ensure accurate representation of the electrostatic environment of the proteins. Protein preparation and structural refinement were performed using AutoDock Vina [34]. The prepared protein structures were subsequently converted into PDBQT format for molecular docking analysis.

2.2. Molecular Docking

Molecular docking analysis was performed to investigate the binding orientation and interaction affinity of the selected natural compounds against the SARS-CoV-2 target proteins. Docking simulations were carried out using AutoDock Vina [34] to evaluate ligand binding within the active sites of 7XJW, 8DRW, and 9PFH. The docking grid boxes were generated around the co-crystallized ligand-binding regions to ensure accurate targeting of the active sites. During the docking simulations, the ligands were treated as flexible while the receptor structures were maintained rigid. The exhaustiveness parameter was set to 8 to ensure adequate conformational sampling, and multiple binding poses were retained for analysis.

The resulting docked complexes were analyzed based on binding affinity and interaction profiles. The best-performing ligand-protein complexes were further visualized and analyzed using PyMOL [35,36] and the ProteinPlus server [37] to identify key intermolecular interactions, including hydrogen bonds, hydrophobic contacts, and active-site interactions. The ligand exhibiting the most favorable and stable interaction profile across the investigated targets was selected for subsequent molecular dynamics simulation studies.

2.3. Molecular Dynamics Simulations

Molecular dynamics (MD) simulations were performed using the GROMACS package [38,39] to investigate the structural stability, conformational behavior, and interaction persistence of the selected apo and ligand-bound SARS-CoV-2 protein systems. The CHARMM force field [40,41] was employed for protein parameterization, while ligand topologies were generated using the SwissParam server [42]. Each protein-ligand complex was solvated in a cubic simulation box using the TIP3P water model [43], and appropriate sodium and chloride ions were added to neutralize the systems under periodic boundary conditions.

Energy minimization was performed using the steepest-descent algorithm [44,45] to remove steric clashes and optimize the system geometry. The systems were subsequently equilibrated under NVT and NPT ensembles [46] at 300 K and 1 bar pressure, respectively. Following equilibration, 100 ns production simulations were conducted under stable thermodynamic conditions. Long-range electrostatic interactions were treated using the Particle Mesh Ewald (PME) method [47,48] with a cutoff distance of 1.0 nm for both electrostatic and van der Waals interactions. The LINCS algorithm [49–51] was applied to constrain hydrogen bonds, and a time step of 2 fs was maintained throughout the simulations.

 doi:10.20944/preprints202606.0440.v1

Trajectory analyses were performed to evaluate key structural parameters including root mean square deviation (RMSD), root mean square fluctuation (RMSF), radius of gyration (Rg), solvent accessible surface area (SASA), and hydrogen bond persistence to assess structural stability and conformational dynamics of the complexes.

2.4. Free Energy Landscape Analysis

Free energy landscape (FEL) analysis was performed to investigate the conformational stability and energy distribution of the apo and ligand-bound SARS-CoV-2 systems following molecular dynamics simulations. The FEL maps were generated using the first two principal components (PC1 and PC2) obtained from principal component analysis (PCA), which describe the dominant collective motions of the protein systems during the simulation trajectory [52,53].

Prior to analysis, trajectory files were corrected for periodic boundary conditions and aligned to reference structures to eliminate rotational and translational motions [54]. Covariance matrices were constructed based on the Cα atomic coordinates, followed by calculation of eigenvectors and eigenvalues to obtain the principal components [55]. The free energy associated with each conformational state was calculated using the thermodynamic relationship shown in equation 1 [56]:

$$\Delta G = -RT \ln P \quad (1)$$

where ΔG represents the free energy, R is the universal gas constant, T is the absolute temperature, and P is the probability of occurrence of a given conformation. The resulting FEL maps were used to evaluate conformational transitions, stability basins, and the effect of ligand binding on the thermodynamic stability of the SARS-CoV-2 target proteins.

2.5. Binding Free Energy Calculation by MMPBSA

Binding free energy calculations were performed using the Molecular Mechanics Poisson-Boltzmann Surface Area (MM-PBSA) method [57,58] to estimate the binding affinity of Amentoflavone toward the SARS-CoV-2 target proteins. Representative frames were extracted from the equilibrated portions of the molecular dynamics trajectories and subjected to MM-PBSA calculations using the g_mmpbsa package integrated with GROMACS [38,39]. The total binding free energy was calculated using the following relationship (Equation 2):

$$\Delta G\_{bind} = \Delta G\_{complex} + (\Delta G\_{protein} + \Delta G\_{ligand}) \quad (2)$$

where ΔG_bind represents the total binding free energy, while G_complex, G_protein, and G_ligand represent the free energies of the complex, protein, and ligand, respectively. The total binding energy was further decomposed into van der Waals, electrostatic, polar solvation, and nonpolar solvation energy contributions to identify the major driving forces responsible for ligand stabilization within the receptor binding pockets. Residue-wise energy decomposition analysis was additionally performed to identify key amino acid residues contributing significantly to protein-ligand interaction stability.

3. Results

3.1. Docking Analysis

Molecular docking analysis was performed to evaluate the binding orientation, interaction strength, and inhibitory potential of selected natural compounds against the SARS-CoV-2 target proteins 7XJW, 8DRW, and 9PFH, thereby identifying compounds capable of forming stable interactions within the receptor active sites.

3.1.1. Binding Affinity of SARS-CoV-2 Target with Selected Natural Compounds

The docking results revealed that most of the investigated compounds exhibited favorable binding affinities (Figure 2), with binding energies ranging from approximately -5.4 to -9.5 kcal/mol, indicating appreciable interaction potential within the active sites of the viral proteins. Among all screened ligands, Amentoflavone (C15) consistently demonstrated the strongest binding affinity toward the three SARS-CoV-2 targets, with docking scores of -9.5 kcal/mol against 7XJW, -9.1

 doi:10.20944/preprints202606.0440.v1

kcal/mol against 8DRW, and -8.6 kcal/mol against 9PFH. The highly negative binding energies observed for Amentoflavone suggest the formation of thermodynamically stable protein-ligand complexes characterized by strong intermolecular interactions within the receptor binding pockets.

The superior binding performance of Amentoflavone may be attributed to its biflavonoid structural framework, which contains multiple hydroxyl groups and extended conjugated aromatic rings capable of establishing diverse non-covalent interactions with amino acid residues located within the catalytic sites of the proteins [59]. The hydroxyl functionalities enhance hydrogen-bond formation with polar residues, whereas the aromatic moieties facilitate hydrophobic interactions and π-π stacking with hydrophobic and aromatic amino acids lining the active pocket [60]. These interaction patterns improve ligand accommodation and molecular complementarity, thereby enhancing complex stability and binding affinity. Furthermore, the rigid polyphenolic backbone of Amentoflavone may minimize conformational fluctuations during binding, contributing to its favorable docking orientation and interaction persistence.

Several other compounds also demonstrated promising binding affinities against one or more target proteins. Quercetin (C18) exhibited strong binding toward 8DRW with a docking score of -8.6 kcal/mol, while Tingenone (C13) showed favorable interactions with 9PFH (-8.1 kcal/mol) and 8DRW (-7.9 kcal/mol). Similarly, Mimulone (C16) and Psoralidin (C9) displayed relatively stable interaction profiles across the investigated targets. In contrast, Hirsutenone (C12) and Curcumin (C7) showed comparatively weaker binding affinities toward certain proteins, suggesting reduced interaction stability within the receptor active sites.

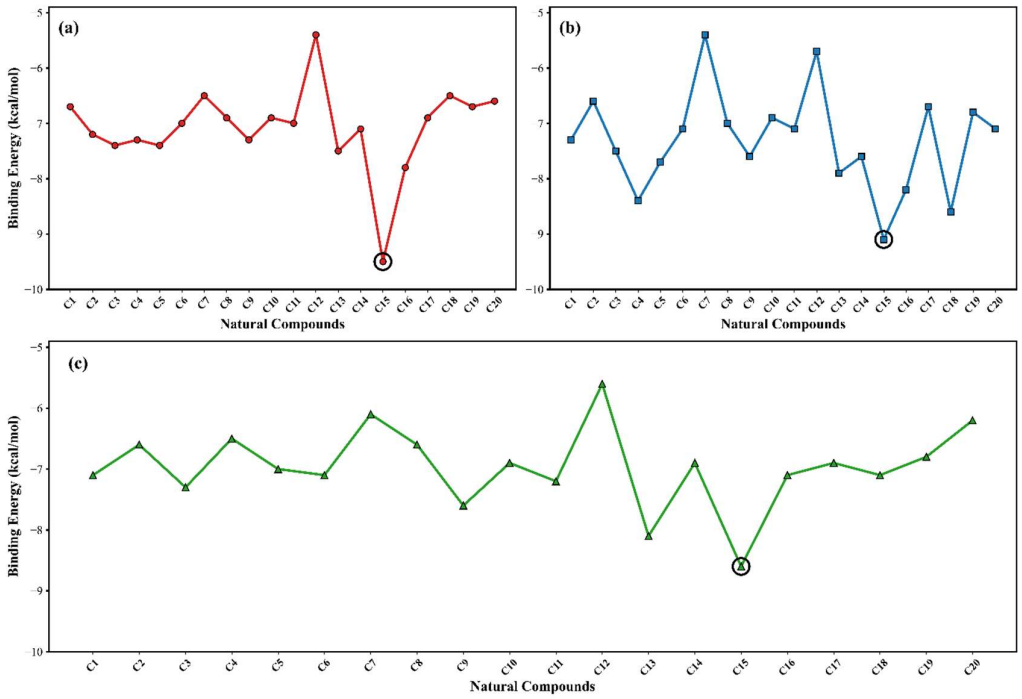

Figure 2. Binding energy of (a) 7XJW, (b) 8DRWand (c) 9PFH SARS-CoV-2 Target with Selected Natural Compounds where C1 is (Pristimerin), C2 (Hesperetin), C3 (Diplacone), C4 (Luteolin), C5 (Bavachinin), C6 (Betulinic acid), C7 (Curcumin), C8 (Rosmariquinone), C9 (Psoralidin), C10 (Cryptotanshinone), C11 (Iguesterin), C12 (Hirsutenone), C13 (Tingenone), C14 (Apigenin), C15 (Amentoflavone), C16 (Mimulone), C17 (Celastrol), C18 (Quercetin), C19 (Methyl tanshinonate), and C20 (Savinin).

Importantly, the consistent high binding affinity of Amentoflavone across all investigated SARS-CoV-2 proteins suggests its potential as a promising multi-target antiviral candidate. Consequently, Amentoflavone was selected for interaction visualization and subsequent molecular dynamics

 doi:10.20944/preprints202606.0440.v1

simulation studies to further investigate the structural stability, conformational behavior, and persistence of the protein-ligand complexes under dynamic physiological conditions.

3.1.2. Docking Interaction Analysis of Amentoflavone with SARS-CoV-2 Targets

Docking interaction analysis was performed to investigate the binding orientation and intermolecular interactions of Amentoflavone within the active sites of the SARS-CoV-2 target proteins 7XJW, 8DRW, and 9PFH. As illustrated in Figures 3–5, Amentoflavone exhibited stable accommodation within the receptor binding pockets and formed multiple intermolecular interactions with key catalytic and surrounding residues. The interaction patterns observed across the three proteins suggest strong ligand-receptor complementarity and support the potential inhibitory activity of Amentoflavone against SARS-CoV-2 targets. The biflavonoid structure of Amentoflavone, characterized by multiple hydroxyl functionalities and conjugated aromatic rings, appears to play an important role in stabilizing the complexes through hydrogen bonding, hydrophobic interactions, and π-related contacts within the active site regions [61].

For the 7XJW complex, Amentoflavone established four hydrogen-bond interactions involving Val26, Thr47, and Asp186 with bond distances of 2.1 Å, 3.0 Å, 2.1 Å, and 2.6 Å, respectively, as shown in Figure 3.2(a-b). Hydrogen-bond distances below 3.5 Å are generally considered favorable for stable ligand binding, while interactions close to 2.0 Å indicate particularly strong electrostatic stabilization [62]. The interactions with Val26 and Thr47 therefore suggest strong binding persistence within the active site cavity. In addition to hydrogen bonding, hydrophobic interactions with residues including His41, Cys144, Ala141, Gly142, Ile140, and Thr143 further stabilized the ligand orientation within the receptor pocket. The presence of multiple aromatic rings in Amentoflavone likely enhanced hydrophobic complementarity and facilitated efficient accommodation inside the catalytic region of the protein.

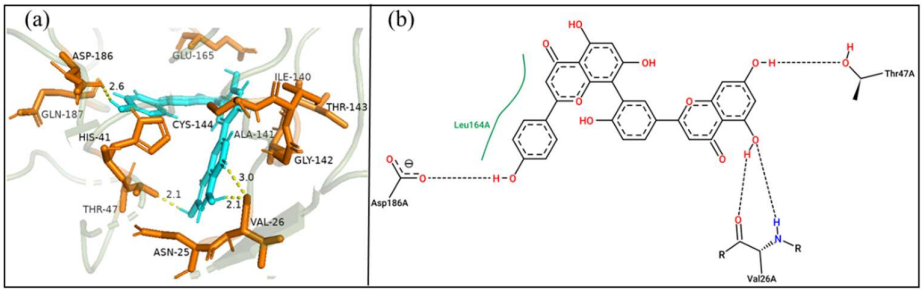

Figure 3. Docking interaction analysis of Amentoflavone with SARS-CoV-2 protein 7XJW showing (a) three-dimensional binding orientation and (b) two-dimensional interaction map illustrating hydrogen-bond and hydrophobic interactions within the active site.

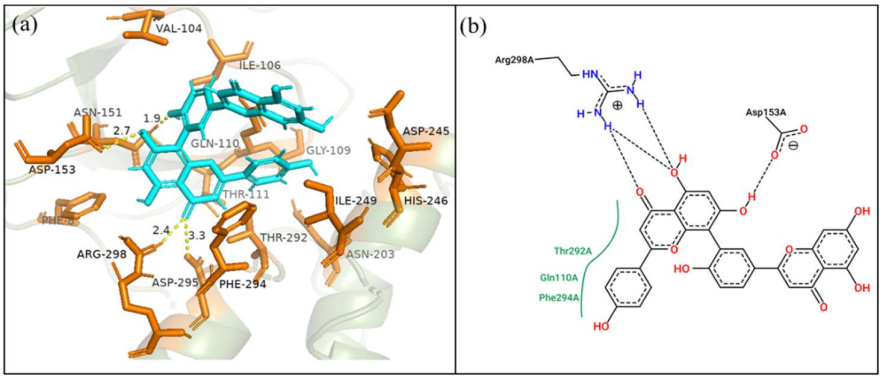

Figure 4. Docking interaction analysis of Amentoflavone with SARS-CoV-2 protein 8DRW showing (a) three-dimensional binding orientation and (b) two-dimensional interaction map displaying intermolecular interactions with surrounding amino acid residues.

 doi:10.20944/preprints202606.0440.v1

Similarly, the 8DRW-Amentoflavone complex demonstrated several favorable hydrogen-bond interactions with Asn151, Asp153, Arg298, and Asp295 at distances of 1.9 Å, 2.7 Å, 2.4 Å, and 3.3 Å, respectively (Figure 3.3a-b). Among these interactions, the hydrogen bond with Asn151 displayed the shortest distance, indicating a strong and highly stable interaction. The simultaneous interaction of Amentoflavone with both acidic and basic residues suggests enhanced electrostatic complementarity within the binding cavity [63]. Additional hydrophobic contacts involving residues such as Gln110, Thr292, and Phe294 further contributed to ligand stabilization and favorable molecular orientation within the active site. Compared with the other complexes, the 8DRW interaction profile exhibited a relatively broader hydrogen-bonding network, which may contribute to improved ligand retention within the receptor environment.

For the 9PFH target, PyMOL analysis identified a hydrogen-bond interaction between Amentoflavone and Gln189 at a distance of 3.0 Å, indicating a stable polar interaction within the binding pocket (Figure 3.4a-b). Further analysis using ProteinPlus revealed two additional hydrogen bonds involving Phe140 and Asn142, demonstrating that the ligand established a more extensive interaction network than initially observed. These additional interactions likely enhance the overall stability of the protein-ligand complex and reinforce ligand accommodation within the receptor cavity. Moreover, hydrophobic interactions involving residues such as Met165 and neighboring aromatic amino acids further stabilized the binding orientation of the ligand.

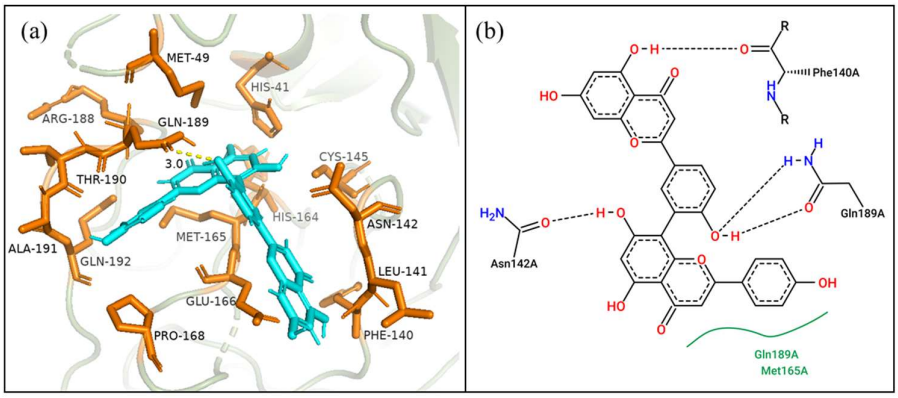

Figure 5. Docking interaction analysis of Amentoflavone with SARS-CoV-2 protein 9PFH showing (a) three-dimensional binding orientation and (b) two-dimensional interaction map illustrating hydrogen-bond and hydrophobic interactions identified using PyMOL and ProteinPlus analyses.

Collectively, the interaction analyses indicate that Amentoflavone forms stable and favorable intermolecular interactions across all investigated SARS-CoV-2 targets. Based on the observed interaction stability and binding orientation, molecular dynamics simulation studies were subsequently performed to further investigate the conformational stability, structural fluctuations, and dynamic behavior of the protein-ligand complexes under physiological conditions.

3.2. Molecular Dynamic Simulation Analysis

Molecular dynamics simulation analysis was performed to evaluate the structural stability, conformational behavior, and dynamic interaction persistence of the apo and protein-ligand complexes under physiological conditions over the simulation trajectory.

3.2.1. Stability and Conformation Analysis

The structural stability and conformational behavior of the apo and Amentoflavone-bound SARS-CoV-2 systems were evaluated using root mean square deviation (RMSD) analysis over a 100 ns molecular dynamics simulation trajectory, as presented in Figure 6(a-b). RMSD is a critical parameter for assessing the overall stability and equilibration of biomolecular systems during

 doi:10.20944/preprints202606.0440.v1

simulation, where lower and less fluctuating RMSD values generally indicate enhanced structural stability and stable ligand accommodation within the receptor binding pocket [64]. The RMSD trajectories demonstrated that all investigated systems attained relatively stable conformations throughout the simulation period, with fluctuations remaining within an acceptable range for globular proteins. The apo7 and complex7 systems exhibited average RMSD values of 0.158 ± 0.021 nm and 0.167 ± 0.023 nm, respectively, indicating that the binding of Amentoflavone induced only minimal conformational perturbation to the 7XJW protein structure. Similarly, apo9 and complex9 displayed average RMSD values of 0.180 ± 0.036 nm and 0.175 ± 0.032 nm, suggesting that ligand binding slightly stabilized the 9PFH system by reducing structural fluctuations relative to the unbound protein. In contrast, apo8 and complex8 exhibited comparatively higher RMSD values of 0.269 ± 0.028 nm and 0.273 ± 0.046 nm, accompanied by broader fluctuations during the simulation trajectory, indicating relatively greater conformational flexibility of the 8DRW system.

The RMSD profiles further revealed distinct dynamic behaviors between the apo and ligand-bound complexes. For the 7XJW and 9PFH systems, the RMSD trajectories of the complexes closely overlapped with their respective apo forms after equilibration, suggesting that Amentoflavone binding did not destabilize the protein structures but instead promoted stable conformational accommodation within the active sites (Figure 6a). The relatively small standard deviation values observed for complex7 and complex9 further support the existence of stable structural dynamics and persistent ligand-protein interactions throughout the simulation period. Conversely, complex8 exhibited comparatively larger RMSD fluctuations and a higher standard deviation, particularly around the mid-simulation region, which may reflect localized conformational rearrangements or increased flexibility within the receptor binding pocket upon ligand binding. Such fluctuations are not necessarily unfavorable, as moderate flexibility may facilitate adaptive binding and dynamic interaction optimization between the ligand and protein residues. However, excessive fluctuations may indicate reduced conformational rigidity and lower structural compactness compared with the other systems [65].

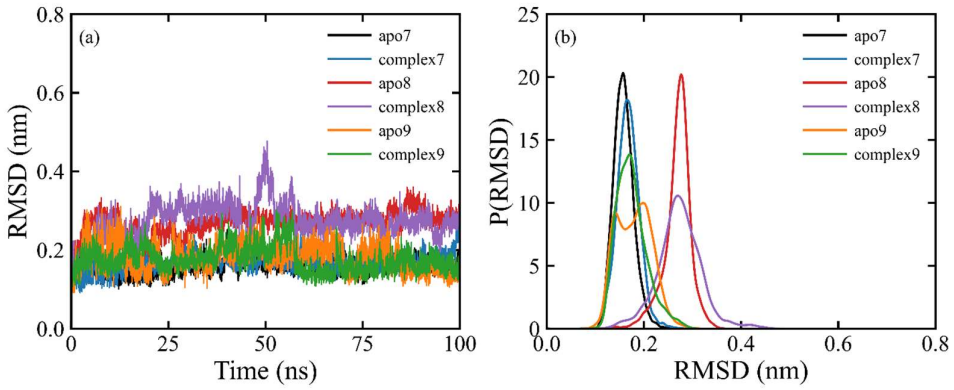

Figure 6. (a) RMSD trajectories and (b) probability density distribution plots of apo and Amentoflavone-bound SARS-CoV-2 protein complexes (7XJW, 8DRW, and 9PFH) during 100 ns molecular dynamics simulations, illustrating the structural stability, conformational fluctuations, and equilibration behavior of the systems.

The probability density distribution analysis presented in Figure 6(b) provides additional insights into the conformational stability and equilibration behavior of the simulated systems. Narrow and sharply defined RMSD distribution peaks are generally associated with stable and well-equilibrated conformational states, whereas broader distributions indicate greater structural heterogeneity and conformational transitions during the simulation [66]. The apo7 and complex7 systems exhibited narrow and highly concentrated RMSD distributions centered around ~0.15-0.18 nm, indicating highly stable and well-equilibrated trajectories. Likewise, complex9 demonstrated a relatively compact distribution profile with slightly lower RMSD values compared with apo9, suggesting improved conformational stabilization following ligand binding. In contrast, the apo8 and

 doi:10.20944/preprints202606.0440.v1

complex8 systems displayed broader RMSD distributions extending toward higher RMSD regions, reflecting increased conformational flexibility and dynamic structural rearrangements. From a drug discovery perspective, the complex7 and complex9 systems appear particularly promising because they combined stable RMSD trajectories, low structural deviations, and well-equilibrated conformational distributions, all of which are desirable characteristics for stable protein-ligand association and sustained inhibitory activity under physiological conditions. Collectively, these findings indicate that Amentoflavone maintained stable binding throughout the simulation period and may serve as a promising lead compound for further antiviral drug development against SARS-CoV-2 targets.

3.2.2. Root Mean Square Fluctuation Analysis

Root mean square fluctuation (RMSF) analysis was performed to evaluate residue-level flexibility and conformational mobility of the apo and Amentoflavone-bound SARS-CoV-2 protein systems throughout the molecular dynamics simulation trajectory. As presented in Figure 7, the majority of residues in all investigated systems exhibited relatively low fluctuation values, generally below 0.20 nm, indicating overall structural stability and maintenance of compact protein conformations during the simulation period. The comparatively lower fluctuations observed within the core regions of the proteins suggest preservation of essential secondary structural elements, including α-helices and β-sheets, which are important for maintaining active-site integrity and stable ligand accommodation [67]. Furthermore, the ligand-bound systems, particularly complex7 and complex9, demonstrated slightly reduced fluctuations compared with their respective apo forms across several residue regions, indicating that Amentoflavone contributed to local structural stabilization through persistent intermolecular interactions within the binding pockets.

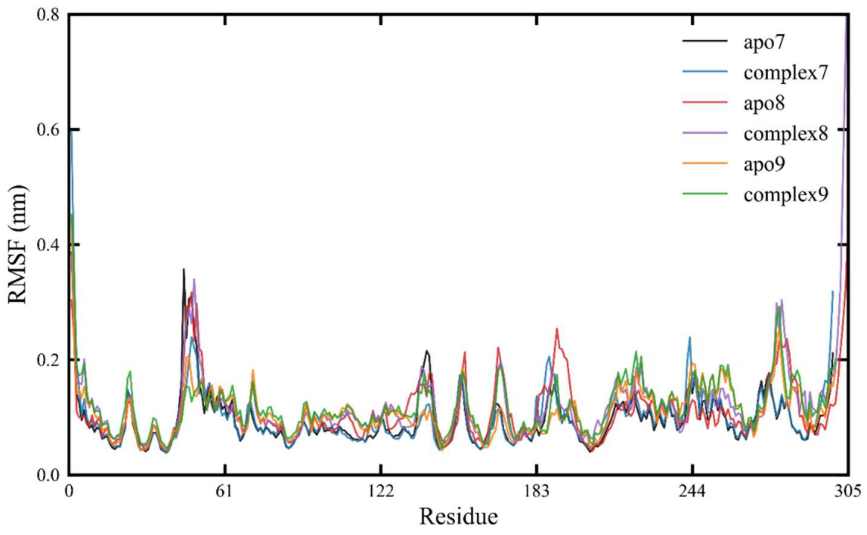

Figure 7. Root mean square fluctuation (RMSF) profiles of apo and Amentoflavone-bound SARS-CoV-2 protein systems (7XJW, 8DRW, and 9PFH) during 100 ns molecular dynamics simulations, illustrating residue-level flexibility, conformational mobility, and the effect of ligand binding on protein structural stability.

Higher fluctuation peaks were primarily observed in loop and terminal regions, especially around residues 40-55, 130-150, 180-200, and near the C-terminal region approaching residue 305. Such regions are generally solvent-exposed and intrinsically flexible due to reduced structural constraints [68]. Among the investigated systems, complex8 displayed relatively greater fluctuations in certain loop regions compared with the other complexes, suggesting increased conformational adaptability during ligand binding. Moderate flexibility within these regions may facilitate induced-fit interactions and dynamic optimization of ligand accommodation within the receptor cavity [65].

 doi:10.20944/preprints202606.0440.v1

From a drug discovery perspective, the reduced residue mobility and maintained structural integrity observed in complex7 and complex9 indicate stable ligand binding and favorable conformational behavior under physiological conditions. Collectively, the RMSF results suggest that Amentoflavone maintained stable interactions with the investigated SARS-CoV-2 targets while preserving overall protein stability, further supporting its potential as a promising multi-target antiviral candidate.

3.2.3. Solvent Accessible Surface Area Analysis

Solvent accessible surface area (SASA) analysis was performed to evaluate the surface exposure, compactness, and conformational stability of the apo and Amentoflavone-bound SARS-CoV-2 protein systems during the 100 ns molecular dynamics simulations. SASA is an important parameter for assessing the extent of protein surface exposure to the solvent environment, where lower fluctuations generally indicate enhanced structural compactness and stable folding behavior [69]. As illustrated in Figure 8(a-b), all investigated systems maintained relatively stable SASA profiles throughout the simulation trajectory, suggesting preservation of overall protein structural integrity upon ligand binding. The apo7 and complex7 systems exhibited closely related average SASA values of 147.313 ± 2.762 nm² and 147.605 ± 2.068 nm², respectively, indicating that Amentoflavone binding induced minimal alteration in the solvent exposure of the 7XJW protein. Similarly, the apo9 and complex9 systems showed moderate SASA values, while the apo8 and complex8 systems displayed comparatively higher solvent-accessible surface areas, suggesting relatively greater surface exposure and conformational flexibility of the 8DRW system.

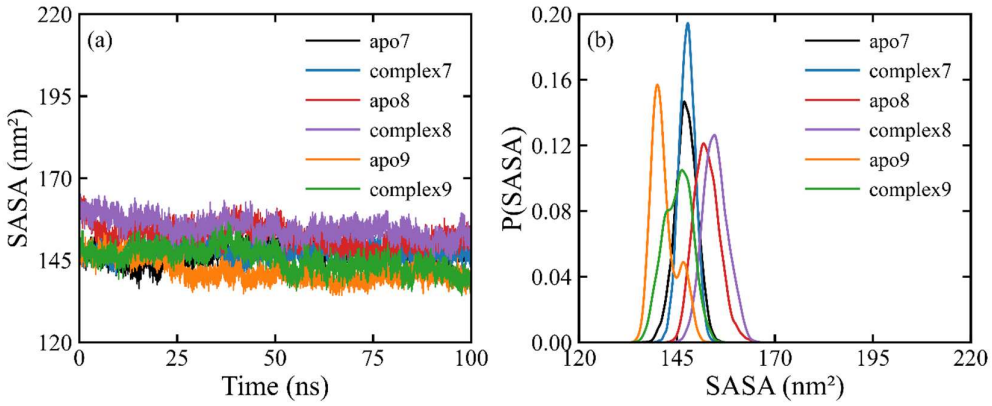

Figure 8. (a) Solvent accessible surface area (SASA) trajectories and (b) probability density distribution plots of apo and Amentoflavone-bound SARS-CoV-2 protein systems (7XJW, 8DRW, and 9PFH) during 100 ns molecular dynamics simulations, illustrating protein surface exposure, structural compactness, and conformational stability upon ligand binding.

The probability density distribution plots further demonstrated narrow and well-defined SASA distributions for most systems, indicating stable equilibration and limited structural expansion during the simulation period (Figure 8b). Notably, complex7 exhibited one of the narrowest distributions and the lowest standard deviation among the complexes, suggesting enhanced compactness and stable ligand accommodation within the receptor binding pocket. In contrast, complex8 displayed slightly broader SASA distributions and higher average SASA values, reflecting increased solvent exposure and greater conformational flexibility upon ligand binding. Although moderate flexibility may support adaptive ligand binding, excessive solvent exposure can reduce structural compactness and interaction persistence [70]. From a drug discovery perspective, the complex7 system appears particularly promising due to its balanced SASA profile, reduced fluctuations, and maintained structural compactness following ligand binding, all of which are desirable characteristics for stable protein-ligand interactions and sustained inhibitory activity under

 doi:10.20944/preprints202606.0440.v1

physiological conditions [70]. Collectively, the SASA results indicate that Amentoflavone binding preserved the structural stability of the investigated SARS-CoV-2 targets while maintaining favorable conformational behavior throughout the simulation trajectory.

3.2.4. Radius of Gyration (Rg) Analysis

The radius of gyration (Rg) analysis was performed to evaluate the structural compactness and folding stability of the apo and Amentoflavone-bound SARS-CoV-2 protein systems during the 100 ns molecular dynamics simulations. Rg is an important parameter for assessing the spatial distribution of atoms around the protein center of mass, where lower and stable Rg values generally indicate compact and structurally stable conformations [71]. As illustrated in Figure 9(a-b), all investigated systems maintained relatively stable Rg trajectories throughout the simulation period, suggesting preservation of overall protein folding and absence of significant structural unfolding upon ligand binding. The apo7 and complex7 systems exhibited nearly identical average Rg values of 2.224 ± 0.012 nm and 2.223 ± 0.010 nm, respectively, indicating that Amentoflavone binding did not induce notable structural expansion or destabilization of the 7XJW protein. Similarly, apo9 and complex9 displayed closely related average Rg values, suggesting maintenance of structural compactness and stable ligand accommodation throughout the simulation trajectory.

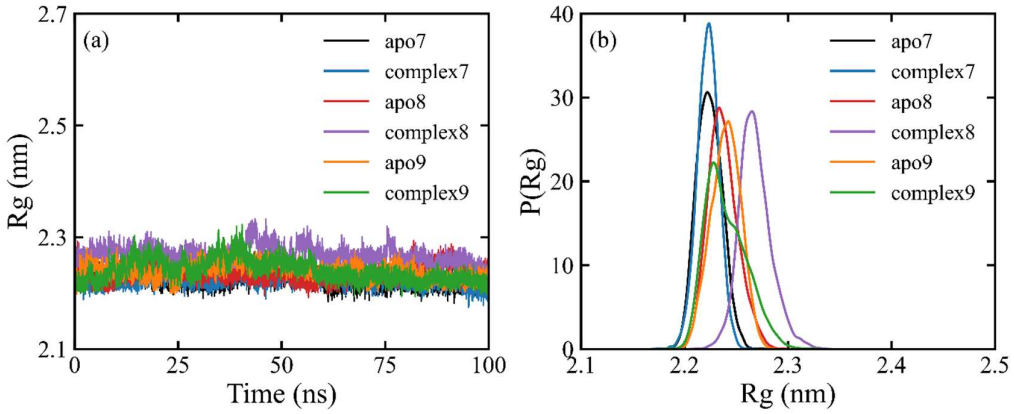

Figure 9. (a) Radius of gyration (Rg) trajectories and (b) probability density distribution plots of apo and Amentoflavone-bound SARS-CoV-2 protein systems (7XJW, 8DRW, and 9PFH) during 100 ns molecular dynamics simulations, illustrating structural compactness, folding stability, and conformational behavior upon ligand binding.

In contrast, the complex8 system exhibited a slightly higher average Rg value (2.268 ± 0.016 nm) compared with apo8 (2.237 ± 0.014 nm), indicating moderate structural expansion and increased conformational flexibility upon ligand binding. This behavior may reflect adaptive rearrangements within the protein structure to optimize intermolecular interactions with Amentoflavone. The probability density distributions shown in Figure 9(b) further demonstrated narrow and well-defined Rg peaks for most systems, indicating stable equilibration and limited conformational heterogeneity during the simulations. Notably, complex7 exhibited one of the narrowest distribution profiles and the lowest standard deviation, suggesting enhanced structural compactness and stable protein-ligand interactions. From a drug discovery perspective, the complex7 and complex9 systems appear particularly favorable because they maintained compact conformations with minimal structural perturbation following ligand binding, characteristics that are desirable for stable inhibitory interactions and sustained biological activity under physiological conditions [72]. Collectively, the Rg analysis indicates that Amentoflavone binding preserved the folding stability and compact structural organization of the investigated SARS-CoV-2 proteins throughout the simulation period.

 doi:10.20944/preprints202606.0440.v1

3.2.5. Hydrogen Bond Analysis

Hydrogen bond analysis was performed to evaluate the interaction persistence, binding stability, and dynamic intermolecular behavior of the Amentoflavone-bound SARS-CoV-2 protein complexes throughout the 100 ns molecular dynamics simulations. Hydrogen bonds are among the most critical non-covalent interactions governing ligand recognition, specificity, and long-term stability within protein binding pockets. As illustrated in Figures 10 and 11, the investigated complexes exhibited distinct hydrogen-bonding behaviors over the simulation trajectory. Complex7 maintained relatively stable hydrogen-bond interactions throughout the simulation with a mean hydrogen bond count of 2.34 and an average occupancy of 99.53%, indicating persistent ligand retention within the active site. The hydrogen-bond occupancy remained consistently above 98% across all sampled intervals, demonstrating highly stable intermolecular interactions. Notably, the average number of hydrogen bonds increased during the later simulation stages, reaching 2.74 within the 80-100 ns interval, suggesting progressive stabilization and improved ligand accommodation during the equilibration process.

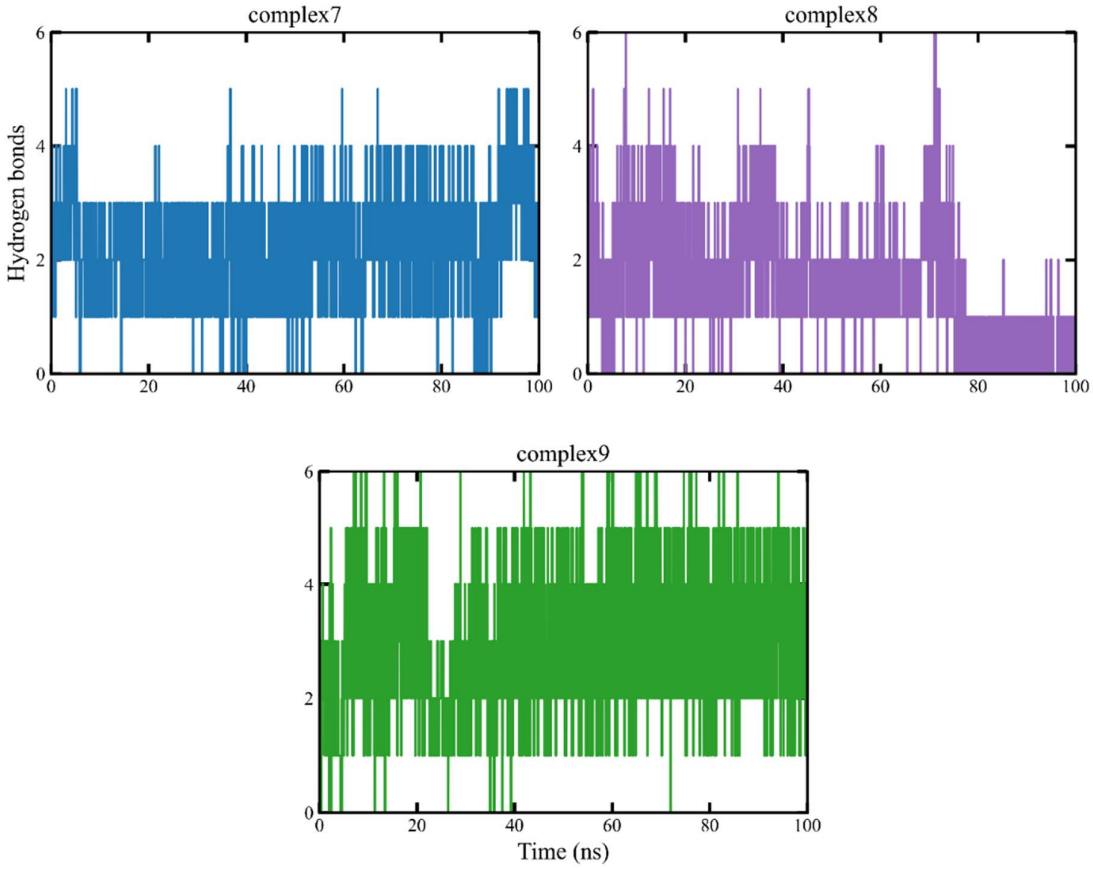

Figure 10. Time evolution of hydrogen bonds formed between Amentoflavone and SARS-CoV-2 protein complexes (complex7, complex8, and complex9) during 100 ns molecular dynamics simulations, illustrating interaction persistence and temporal stability of ligand-protein hydrogen-bond networks.

Among the investigated systems, complex9 exhibited the strongest and most persistent hydrogen-bonding network, with a mean hydrogen bond count of 3.00 and an average occupancy of 99.72%. The complex maintained exceptionally high occupancies approaching 100% throughout nearly all simulation windows, particularly between 40-100 ns where the occupancy reached 100% in several intervals. In addition, the average number of hydrogen bonds increased steadily during the simulation, reaching values above 3.0 during the final stages, indicating highly stable and continuous

 doi:10.20944/preprints202606.0440.v1

ligand-protein interactions. The strong hydrogen-bond persistence observed in complex9 may be associated with the multiple hydroxyl groups present in the biflavonoid structure of Amentoflavone, which facilitate repeated donor-acceptor interactions with polar residues within the receptor cavity [61,62]. Such persistent hydrogen bonding is highly desirable in drug discovery because it enhances ligand residence time, stabilizes binding orientation, and may improve inhibitory efficiency under physiological conditions.

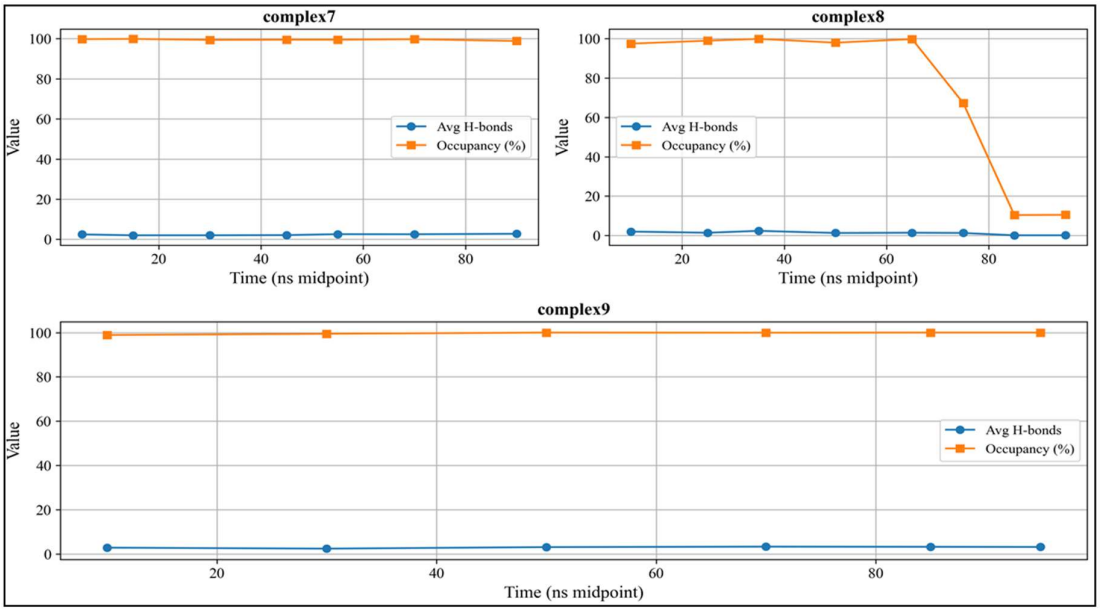

Figure 11. Average hydrogen bond number and occupancy percentage of Amentoflavone-bound SARS-CoV-2 protein complexes across different simulation time windows, demonstrating the persistence, stability, and dynamic behavior of intermolecular hydrogen-bond interactions during the molecular dynamic simulations.

In contrast, complex8 demonstrated comparatively lower interaction persistence, with a mean hydrogen bond count of 1.24 and an average occupancy of 72.80%. Although the system exhibited strong occupancies above 97% during the early and middle simulation intervals, a substantial decline was observed after 70 ns, where occupancy decreased to approximately 10% during the 80-100 ns period. This reduction was accompanied by a marked decrease in average hydrogen bond count, suggesting partial disruption of ligand-protein interactions and increased conformational flexibility within the binding pocket. Such behavior may reflect dynamic structural rearrangements that weakened ligand retention during the later simulation stages. From a drug discovery perspective, complex9 appears to be the most promising system due to its sustained hydrogen-bond network, consistently high occupancy, and stable intermolecular interaction profile throughout the simulation trajectory. Collectively, the hydrogen bond analysis demonstrates that Amentoflavone maintained persistent and favorable interactions with the investigated SARS-CoV-2 proteins, particularly in complex7 and complex9, supporting its potential as a stable multi-target antiviral candidate.

3.3. Free Energy Landscape (FEL) Analysis

Free energy landscape (FEL) analysis was performed to investigate the conformational stability, energy distribution, and structural transition behavior of the apo and Amentoflavone-bound SARS-CoV-2 protein systems during the molecular dynamics simulations. The FEL plots were constructed using principal component analysis (PCA), where the low-energy regions represent thermodynamically stable conformational states, while broader and dispersed energy basins indicate increased conformational flexibility and structural transitions [55,73,74]. As illustrated in Figure 12(a-f), the apo7 and complex7 systems exhibited relatively compact and concentrated low-energy basins,

 doi:10.20944/preprints202606.0440.v1

suggesting stable conformational sampling and restricted structural fluctuations throughout the simulation trajectory. In particular, complex7 demonstrated a well-defined and localized energy minimum with limited conformational dispersion compared with apo7, indicating that Amentoflavone binding promoted a more thermodynamically stable conformational state. This observation is consistent with the RMSD, RMSF, and hydrogen-bond analyses, where complex7 exhibited low structural deviations, reduced residue fluctuations, and persistent intermolecular interactions throughout the simulation period. The preservation of a compact energy basin suggests efficient ligand accommodation and stable protein-ligand association under dynamic physiological conditions [55].

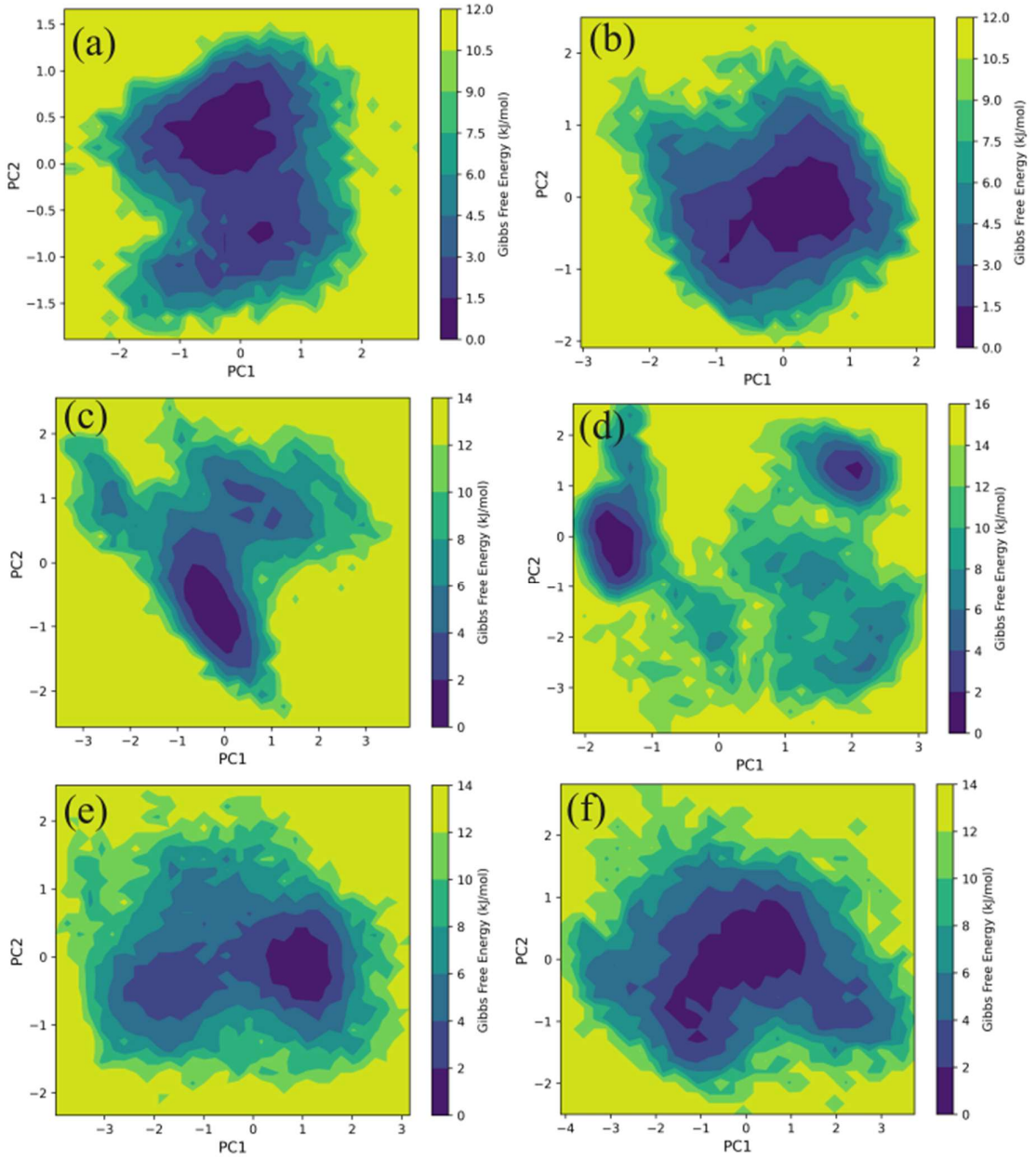

Figure 12. Free energy landscape (FEL) plots of apo and Amentoflavone-bound SARS-CoV-2 protein systems generated from principal component analysis during 100 ns molecular dynamics simulations showing conformational sampling, energy minima, and thermodynamic stability of (a) apo7, (b) complex7, (c) apo8, (d) complex8, (e) apo9, and (f) complex9 systems.

 doi:10.20944/preprints202606.0440.v1

Similarly, the complex9 system displayed relatively stable low-energy conformational states with moderate conformational spread compared with apo9, indicating favorable structural adaptation upon ligand binding. The presence of continuous and connected low-energy regions suggests stable conformational transitions and sustained intermolecular interactions during the simulation [73]. These findings are supported by the hydrogen-bond analysis, where complex9 exhibited the highest hydrogen-bond persistence and occupancy among all investigated systems, indicating highly stable ligand retention within the binding pocket. In contrast, the apo8 and complex8 systems exhibited comparatively broader and more dispersed energy landscapes characterized by multiple minima and wider conformational distributions, reflecting increased structural flexibility and conformational heterogeneity. Although moderate flexibility may facilitate adaptive binding behavior, excessive conformational dispersion may indicate reduced structural compactness and lower thermodynamic stability [75]. From a drug discovery perspective, complex7 and complex9 appear to represent the most favorable systems due to their compact low-energy basins, stable conformational behavior, and consistent interaction persistence throughout the simulations. Collectively, the FEL analysis further confirms that Amentoflavone stabilized the conformational dynamics of the investigated SARS-CoV-2 targets, supporting its potential as a promising multi-target antiviral candidate.

3.4. Binding Free Energy and Decomposition

The MM-PBSA binding free energy analysis provided detailed insights into the thermodynamic stability and intermolecular interaction contributions governing the binding of Amentoflavone to the SARS-CoV-2 target proteins, as presented in Table 1. All investigated systems exhibited negative total binding free energies (ΔG_bind), indicating thermodynamically favorable and spontaneous ligand-protein interactions. Among the complexes, the 7XJW-Amentoflavone system demonstrated the most favorable binding free energy (-89.064 ± 7.152 kJ/mol), followed by 8DRW (-73.798 ± 18.143 kJ/mol) and 9PFH (-71.765 ± 9.143 kJ/mol). This suggests that the 7XJW complex possessed comparatively stronger interaction stability and enhanced binding favorability, consistent with the previous docking, RMSD, hydrogen-bond, and free energy landscape analyses. Energy decomposition further revealed that van der Waals interactions (ΔG_vdW) were the major driving force stabilizing the complexes, with highly negative contributions observed across all systems. These favorable hydrophobic interactions are likely associated with the biflavonoid structure of Amentoflavone, whose extended aromatic rings facilitate strong hydrophobic contacts and π-related interactions with nonpolar residues within the receptor binding pockets [61,63]. In addition, electrostatic interactions (ΔG_elec) contributed significantly to the stabilization of the 7XJW and 9PFH complexes, reflecting the importance of hydrogen bonding and polar interactions mediated by the multiple hydroxyl groups present in the ligand structure.

In contrast, the polar solvation energy (ΔG_polar) contributed unfavorably to binding in all systems, as indicated by the positive energy values. This unfavorable contribution is commonly associated with desolvation penalties arising from disruption of ligand-solvent and protein-solvent interactions during complex formation [76,77]. However, the strong favorable van der Waals and electrostatic contributions effectively compensated for the unfavorable polar solvation energies, resulting in overall stable and energetically favorable complexes. The nonpolar solvation energy (ΔG_nonpol) also contributed favorably, although to a lesser extent, further supporting hydrophobic stabilization within the binding environment. From a drug discovery perspective, the 7XJW-Amentoflavone complex appears to represent the most promising system due to its highly favorable binding free energy, balanced interaction profile, and previously observed conformational stability during molecular dynamics simulations. Collectively, these findings suggest that hydrophobic interactions, hydrogen bonding, and electrostatic complementarity play critical roles in stabilizing Amentoflavone within the receptor active sites, thereby supporting its potential as a promising multi-target antiviral candidate against SARS-CoV-2 proteins.

 doi:10.20944/preprints202606.0440.v1

Table 1. Relative binding free energies (kJ/mol) of the 7XJW, 8DRW and 9PFH against amentoflavone from MMPBSA.

Compound	ΔG_{vdw}(kJ/mol)	ΔG_{elec} (kJ/mol)	ΔG_{polar}(kJ/mol)	ΔG_{nonpol} (kJ/mol)	ΔG_{bind} (kJ/mol)
7XJW	-158.259 ± 14.696	-78.230 ± 9.374	166.197±15.553	-18.772 ± 0.844	-89.064 ± 7.152
8DRW	-172.876 ± 21.602	-19.530 ± 10.265	137.092±23.381	-18.484 ± 1.520	-73.798 ±18.143
9PFH	-165.425 ± 11.461	-61.765 ± 13.243	173.539 ±16.794	-18.114 ± 0.741	-71.765 ± 9.143

ΔG_{bind} = Binding Energy; ΔE_{elec} = **electrostatic energy**; ΔE_{vdW} = **van der Waals**; ΔE_{polar} = **Polar Solvation Energy**; ΔE_{sasa} = **Solvent Accessible Surface Area**.

3.5. Energy Contribution by the Individual Amino Acid Residues

To further elucidate the molecular basis of Amentoflavone binding within the SARS-CoV-2 targets, residue-wise free energy decomposition analysis was performed to identify the key amino acid residues contributing to complex stabilization, as illustrated in Figure 13(a-c). The analysis revealed that several residues within the receptor binding pockets contributed favorably through strong hydrophobic and electrostatic interactions with the ligand. In the 7XJW complex, residues including Leu164, Met190, Glu165, Cys144, Leu27, Val42, and His41 exhibited notable negative energy contributions, with Leu164 and Met190 showing the strongest stabilizing effects. These residues are predominantly hydrophobic or moderately polar in nature, suggesting that van der Waals interactions and hydrophobic complementarity played major roles in stabilizing the ligand within the active site [78]. Similarly, the 8DRW complex showed favorable contributions from residues such as Phe294, Ile249, Asp245, Asp248, Gln107, and Gln110, where Phe294 exhibited the strongest contribution. The presence of aromatic and charged residues within the binding cavity likely enhanced both hydrophobic stabilization and electrostatic interactions with the hydroxyl-rich biflavonoid scaffold of Amentoflavone [79]. In contrast, the 9PFH system demonstrated comparatively fewer dominant interacting residues, with Met165, Gln189, Pro168, and Met49 contributing significantly to ligand stabilization, particularly through hydrophobic contacts and hydrogen-bond interactions.

The residue decomposition profile further supports the findings obtained from molecular docking, hydrogen-bond, and MM-PBSA analyses, where hydrophobic interactions and electrostatic complementarity were identified as the principal driving forces governing complex stability. Notably, the 7XJW complex exhibited the strongest and most distributed favorable residue contributions, indicating enhanced interaction cooperativity within the receptor cavity. The strong contributions from Leu164 and Met190 may explain the highly favorable total binding free energy and stable conformational behavior observed during the molecular dynamic simulations. Although the 8DRW complex displayed several strong residue contributions, the interaction energies appeared more localized and accompanied by comparatively higher structural flexibility, consistent with the broader conformational distributions observed in the RMSD and FEL analyses [80]. Meanwhile, the 9PFH system maintained stable but relatively moderate residue interaction contributions. From a drug discovery perspective, the 7XJW-Amentoflavone complex appears to represent the most promising system due to its balanced residue interaction network, strong hydrophobic stabilization, and favorable energetic contributions across multiple active-site residues. Collectively, the residue-wise energy decomposition analysis highlights the importance of aromatic, hydrophobic, and polar residues in stabilizing Amentoflavone within the receptor binding pockets and further supports its potential as a promising multi-target antiviral lead compound against SARS-CoV-2 proteins.

 doi:10.20944/preprints202606.0440.v1

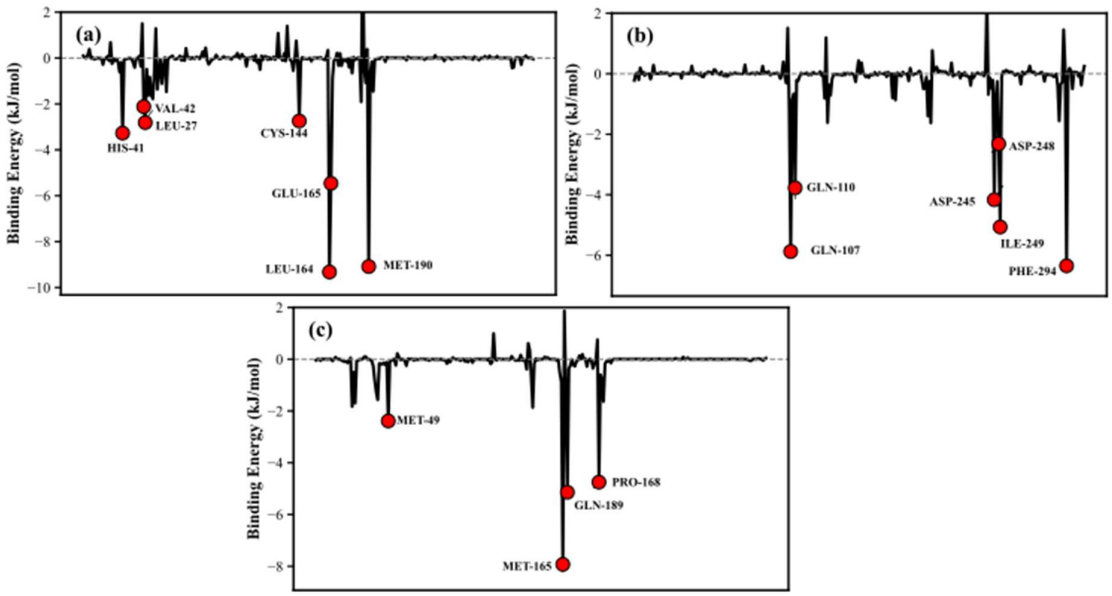

Figure 13. Per-residue binding free energy decomposition profiles of Amentoflavone-bound SARS-CoV-2 protein complexes showing the major amino acid residues contributing to ligand stabilization in (a) 7XJW, (b) 8DRW, and (c) 9PFH systems obtained from MM-PBSA analysis.

4. Discussion

The identification of effective multi-target inhibitors remains an important strategy for combating SARS-CoV-2, particularly in response to the continuous emergence of viral variants and the potential development of drug resistance. In the present study, Amentoflavone exhibited favorable interaction profiles across all investigated viral targets, suggesting broad-spectrum inhibitory potential. The observed binding behavior may be attributed to its biflavonoid architecture, which contains multiple hydroxyl groups and aromatic rings capable of forming extensive hydrogen-bonding and hydrophobic interactions within protein active sites. Similar observations have been reported for flavonoid-based inhibitors of SARS-CoV-2 proteases and replication-associated proteins, where polyphenolic scaffolds enhanced ligand–protein complementarity and binding stability [20,21].

The molecular dynamics simulations further demonstrated that Amentoflavone remained stably accommodated within the receptor cavities while preserving the structural integrity of the proteins. Stable conformational behavior, limited structural deviations, and persistent intermolecular interactions are generally regarded as indicators of effective target engagement and prolonged inhibitory activity under physiological conditions [64,67]. Moreover, the compact low-energy conformational basins observed in the free energy landscape analysis suggest that ligand binding promoted thermodynamically favorable conformational states, consistent with previous studies reporting enhanced stability of antiviral protein-ligand complexes occupying restricted energy minima [73,74].

The favorable MM-PBSA binding energies further revealed that van der Waals and electrostatic interactions were the primary driving forces governing complex stabilization. This observation agrees with previous computational investigations demonstrating that hydrophobic contacts and hydrogen-bond networks are critical determinants of flavonoid-mediated inhibition of SARS-CoV-2 proteins [61,76]. Collectively, these findings highlight Amentoflavone as a promising multi-target antiviral scaffold and provide a strong computational basis for subsequent in vitro and in vivo validation studies aimed at developing novel therapeutic interventions against COVID-19.

 doi:10.20944/preprints202606.0440.v1

5. Conclusions

This study employed an integrated computational strategy combining molecular docking, molecular dynamics simulations, free energy landscape analysis, hydrogen-bond evaluation, and MM-PBSA calculations to investigate the inhibitory potential of natural bioactive compounds against the SARS-CoV-2 target proteins 7XJW, 8DRW, and 9PFH. Among the screened compounds, Amentoflavone consistently demonstrated superior interaction behavior and favorable binding characteristics across all investigated systems. Molecular docking analysis revealed stable binding orientations supported by strong hydrogen-bond and hydrophobic interactions within the receptor active sites. Subsequent molecular dynamics simulations confirmed that the ligand-bound complexes maintained stable conformational behavior, compact structural organization, and persistent intermolecular interactions throughout the 100 ns simulation period. The RMSD, RMSF, SASA, radius of gyration, and hydrogen-bond analyses collectively indicated that Amentoflavone binding did not destabilize the protein structures but instead promoted stable ligand accommodation and interaction persistence under physiological conditions.

Furthermore, free energy landscape and MM-PBSA analyses demonstrated that the binding of Amentoflavone was thermodynamically favorable and primarily driven by van der Waals and electrostatic interactions. Residue-wise energy decomposition further identified several hydrophobic and polar residues that contributed significantly to ligand stabilization within the receptor cavities. Among the investigated systems, the 7XJW-Amentoflavone complex exhibited the most favorable energetic and dynamic stability profile, suggesting enhanced inhibitory potential relative to the other targets. Overall, the findings of this study highlight the therapeutic promise of Amentoflavone as a potential multi-target SARS-CoV-2 inhibitor and provide a valuable computational framework for accelerating antiviral drug discovery. Nevertheless, further in vitro and in vivo investigations are required to validate the biological activity, pharmacological efficacy, and clinical applicability of the proposed compound.

Author Contributions: Yoshua B. Mtulo: Methodology, Investigation, Formal analysis, Data curation, Conceptualization. Angelina. I. Makaye: Methodology, Investigation, Investigation, Formal analysis. Fidele Ntie-Kang: Investigation, Formal analysis, Data curation. Lucas Paul: Writing original draft, Visualization, Methodology, Investigation, Formal analysis, Data curation, Conceptualization. All authors have read and agreed to the published version of the manuscript.

Funding: No external funding.

Institutional Review Board Statement: Not applicable.

Informed Consent Statement: Not applicable.

Acknowledgments: We thank Almighty God for His guidance throughout this study.

Conflicts of Interest: All authors declare no conflict of interest.

Abbreviations

The following abbreviations are used in this manuscript:

SARS-CoV-2	Severe Acute Respiratory Syndrome Coronavirus 2
MD	Molecular Dynamic
RMSF	Root Mean Square Fluctuation
RMSD	Root Mean Square Deviation
SASA	Solvent Accessible Surface Area
Rg	Radius of Gyration

References

1. O. Abdulmajed, Clinical Implications and Evaluations of Pandemic Disease (COVID-19) in TURKEY (2021) 225.

 doi:10.20944/preprints202606.0440.v1

2. A.A. Hammadi, M.R.R. Al-Mousawi, Int. J. Pharm. Sci. Drug Res (2021).
3. W.H.O.M.-C.R. Group, PLoS Curr. 5 (2013) ecurrents-outbreaks.
4. S. Al Hajjar, Z.A. Memish, K. Mcintosh, Ann. Saudi Med. 33 (2013) 427–436.
5. N. Ramadan, H. Shaib, Germs 9 (2019) 35.
6. N.C. Peeri, N. Shrestha, M.S. Rahman, R. Zaki, Z. Tan, S. Bibi, M. Baghbanzadeh, N. Aghamohammadi, W. Zhang, U. Haque, Int. J. Epidemiol. 49 (2020) 717–726.
7. O.P. Mehta, P. Bhandari, A. Raut, S.E.O. Kacimi, N.T. Huy, Front. Public Health 8 (2021) 582932.
8. G.D. Hughes, O.N. Mbamalu, C.O. Okonji, T.R. Puoane, J. Racial Ethn. Health Disparities 9 (2022) 376–383.
9. A.T. Levin, N. Owusu-Boaitey, S. Pugh, B.K. Fosdick, A.B. Zwi, A. Malani, S. Soman, L. Besançon, I. Kashnitsky, S. Ganesh, BMJ Glob. Health 7 (2022).
10. J.O. Arowoogun, J.O. Ogugua, I.P. Odilibe, C. Onwumere, E.C. Anyanwu, O. Akomolafe, World Journal of Advanced Research and Reviews 21 (2024) 2729–2739.
11. T. Dzinamarira, M. Dzobo, I. Chitungo, J. Med. Virol. 92 (2020) 2465–2472.
12. M. Shammi, M. Bodrud-Doza, A.R.M.T. Islam, M.M. Rahman, Heliyon 6 (2020).
13. V.P. Chavda, S. Vuppu, T. Mishra, S. Kamaraj, A.B. Patel, N. Sharma, Z.-S. Chen, Pharmacological Reports 74 (2022) 1120–1148.
14. V.S. Salian, J.A. Wright, P.T. Vedell, S. Nair, C. Li, M. Kandimalla, X. Tang, E.M. Carmona Porquera, K.R. Kalari, K.K. Kandimalla, Mol. Pharm. 18 (2021) 754–771.
15. J. Gerhart, D.S. Cox, R.S.P. Singh, P.L.S. Chan, R. Rao, R. Allen, H. Shi, J.C. Masters, B. Damle, Clin. Pharmacokinet. 63 (2024) 27.
16. C. Marzolini, D.R. Kuritzkes, F. Marra, A. Boyle, S. Gibbons, C. Flexner, A. Pozniak, M. Boffito, L. Waters, D. Burger, Clin. Pharmacol. Ther. 112 (2022) 1191–1200.
17. S.M.R. Hashemian, A. Sheida, M. Taghizadieh, M.Y. Memar, M.R. Hamblin, H.B. Baghi, J.S. Nahand, Z. Asemi, H. Mirzaei, Biomedicine & Pharmacotherapy 162 (2023) 114367.
18. S. Patil, G. Narwade, G. Gondhali, Journal of Applied Sciences and Clinical Practice 4 (2023) 136–140.
19. Y. Guo, A. Ma, X. Wang, C. Yang, X. Chen, G. Li, F. Qiu, Front. Chem. 10 (2022) 1005360.
20. B.A. Gomes, D.A. Fernandes, T.S. da Fonseca, M.F. Campos, P.A. Jural, M.V. Toledo e Silva, L.E.C. Constant, A.A.S. da Veiga, B.R. Ferreira, E.S. Magalhães, Drugs and Drug Candidates 4 (2025) 27.
21. M. Omrani, M. Keshavarz, S. Nejad Ebrahimi, M. Mehrabi, L.J. McGaw, M. Ali Abdalla, P. Mehrbod, Front. Pharmacol. 11 (2021) 586993.
22. J. Alijotas-Reig, E. Esteve-Valverde, C. Belizna, A. Selva-O'Callaghan, J. Pardos-Gea, A. Quintana, A. Mekinian, A. Anunciacion-Llunell, F. Miró-Mur, Autoimmun. Rev. 19 (2020) 102569.
23. M. Asif, M. Saleem, M. Saadullah, H.S. Yaseen, R. Al Zarzour, Inflammopharmacology 28 (2020) 1153–1161.
24. H.M. Berman, T. Battistuz, T.N. Bhat, W.F. Bluhm, P.E. Bourne, K. Burkhardt, Z. Feng, G.L. Gilliland, L. Iype, S. Jain, Biological Crystallography 58 (2002) 899–907.
25. S. Kim, J. Chen, T. Cheng, A. Gindulyte, J. He, S. He, Q. Li, B.A. Shoemaker, P.A. Thiessen, B. Yu, Nucleic Acids Res. 51 (2023) D1373–D1380.
26. N.M. O'Boyle, C. Morley, G.R. Hutchison, Chem. Cent. J. 2 (2008) 5.
27. L.S. Dodda, I. Cabeza de Vaca, J. Tirado-Rives, W.L. Jorgensen, Nucleic Acids Res. 45 (2017) W331–W336.
28. L. Verlet, Physical Review 159 (1967) 98.
29. C.-Y. Ho, J.-X. Yu, Y.-C. Wang, Y.-C. Lin, Y.-F. Chiu, J.-Y. Gao, S.-J. Lai, M.-J. Chen, W.-C. Huang, N. Tien, Int. J. Mol. Sci. 23 (2022) 5669.
30. M. Bianchi, (2022).
31. S.K. Burley, H.M. Berman, C. Bhikadiya, C. Bi, L. Chen, L. Di Costanzo, C. Christie, K. Dalenberg, J.M. Duarte, S. Dutta, Nucleic Acids Res. 47 (2019) D464–D474.
32. J.-Y. Sgro, Dasher Wustl Edu (2017).
33. E.C. Meng, T.D. Goddard, E.F. Pettersen, G.S. Couch, Z.J. Pearson, J.H. Morris, T.E. Ferrin, Protein Science 32 (2023) e4792.
34. J. Eberhardt, D. Santos-Martins, A.F. Tillack, S. Forli, J. Chem. Inf. Model. 61 (2021) 3891–3898.
35. L. Schrödinger, W. DeLano, (2020).
36. D. Seeliger, B.L. de Groot, J. Comput. Aided. Mol. Des. 24 (2010) 417–422.

 doi:10.20944/preprints202606.0440.v1

37. C. Ehrt, T. Schulze, J. Graef, K. Diedrich, J. Pletzer-Zelgert, M. Rarey, Nucleic Acids Res. 53 (2025) W478–W484.
38. M.J. Abraham, D. Van Der Spoel, E. Lindahl, B. Hess, GROMACS User Manual Version 5 (2016).
39. D. Van Der Spoel, E. Lindahl, B. Hess, G. Groenhof, A.E. Mark, H.J.C. Berendsen, J. Comput. Chem. 26 (2005) 1701–1718.
40. J. Lee, M. Hitzenberger, M. Rieger, N.R. Kern, M. Zacharias, W. Im, J. Chem. Phys. 153 (2020).
41. B.R. Brooks, C.L. Brooks III, A.D. Mackerell Jr, L. Nilsson, R.J. Petrella, B. Roux, Y. Won, G. Archontis, C. Bartels, S. Boresch, J. Comput. Chem. 30 (2009) 1545–1614.
42. M. Bugnon, M. Goullieux, U.F. Rohrig, M.A.S. Perez, A. Daina, O. Michielin, V. Zoete, J. Chem. Inf. Model. 63 (2023) 6469–6475.
43. B. Drossel, Journal of Chemical Physics 140 (2014).
44. J. Fliege, B.F. Svaiter, Mathematical Methods of Operations Research 51 (2000) 479–494.
45. T.E. Abrudan, J. Eriksson, V. Koivunen, IEEE Transactions on Signal Processing 56 (2008) 1134–1147.
46. I.R. McDonald, Mol. Phys. 23 (1972) 41–58.
47. U. Essmann, L. Perera, M.L. Berkowitz, T. Darden, H. Lee, L.G. Pedersen, J. Chem. Phys. 103 (1995) 8577–8593.
48. T. Darden, L. Perera, L. Li, L. Pedersen, Structure 7 (1999) R55–R60.
49. Q. Duan, S.P. Reid, N.R. Clark, Z. Wang, N.F. Fernandez, A.D. Rouillard, B. Readhead, S.R. Tritsch, R. Hodos, M. Hafner, NPJ Syst. Biol. Appl. 2 (2016) 16015.
50. B. Hess, H. Bekker, H.J.C. Berendsen, J.G.E.M. Fraaije, J. Comput. Chem. 18 (1997) 1463–1472.
51. B. Hess, J. Chem. Theory Comput. 4 (2008) 116–122.
52. E.A.F. Martis, E.C. Coutinho, in: Structural Bioinformatics: Applications in Preclinical Drug Discovery Process, Springer, 2019, pp. 1–24.
53. N. Hansen, W.F. Van Gunsteren, J. Chem. Theory Comput. 10 (2014) 2632–2647.
54. P.L. Barclay, D.Z. Zhang, J. Comput. Phys. 435 (2021) 110238.
55. M. Post, S. Wolf, G. Stock, J. Chem. Phys. 150 (2019).
56. L. Boltzmann, in: The Kinetic Theory of Gases: An Anthology of Classic Papers with Historical Commentary, World Scientific, 2003, pp. 262–349.
57. R. Kumari, R. Kumar, O.S.D.D. Consortium, A. Lynn, J. Chem. Inf. Model. 54 (2014) 1951–1962.
58. Z.O. Oresanya, G.C. Eleanya, T.A. Akande, T.M. Jesugbemi, R. Kanmodi, Discover Chemistry 3 (2026) 44.
59. A. Portilla-Martinez, M. Ortiz-Flores, I. Hidalgo, C. Gonzalez-Ruiz, E. Meaney, G. Ceballos, N. Nájera, J. Mol. Model. 28 (2022) 404.
60. K.M. Makwana, R. Mahalakshmi, Protein Science 24 (2015) 1920–1933.
61. V. Tarallo, L. Lepore, M. Marcellini, F. Dal Piaz, L. Tudisco, S. Ponticelli, F.W. Lund, P. Roepstorff, A. Orlandi, C. Pisano, Journal of Biological Chemistry 286 (2011) 19641–19651.
62. S. Sarkhel, G.R. Desiraju, Proteins: Structure, Function, and Bioinformatics 54 (2004) 247–259.
63. X. Xiong, N. Tang, X. Lai, J. Zhang, W. Wen, X. Li, A. Li, Y. Wu, Z. Liu, Front. Pharmacol. 12 (2021) 768708.
64. M. Arnittali, A.N. Rissanou, V. Harmandaris, Procedia Comput. Sci. 156 (2019) 69–78.
65. M.L. Teodoro, L.E. Kavraki, Curr. Pharm. Des. 9 (2003) 1635–1648.
66. A. Biswas, T. Paul, M.I. Hossain, B.S. Bahadur, A. Naher, E. Mitra, A. Majumder, R.C. Das, U. Shill, N.C. Bhowmick, Sci. Rep. (2026).
67. G. Zanotti, Crystallogr. Rev. 29 (2023) 48–75.
68. B.M. Nestl, B. Hauer, ACS Catal. 4 (2014) 3201–3211.
69. S. Ausaf Ali, M. Imtaiyaz Hassan, A. Islam, F. Ahmad, Curr. Protein Pept. Sci. 15 (2014) 456–476.
70. A. Maity, S. Majumdar, P. Priya, P. De, S. Saha, S. Ghosh Dastidar, J. Biomol. Struct. Dyn. 33 (2015) 298–321.
71. M.Y. Lobanov, N.S. Bogatyreva, O. V Galzitskaya, Mol. Biol. 42 (2008) 623–628.
72. I. V Komarov, V.A. Bugrov, A. Cherednychenko, O.O. Grygorenko, The Chemical Record 24 (2024) e202300276.
73. S. Moradi, A. Nowroozi, M.A. Nezhad, P. Jalali, R. Khosravi, M. Shahlaei, Comput. Biol. Med. 183 (2024) 109245.

 doi:10.20944/preprints202606.0440.v1

74. E. Papaleo, P. Mereghetti, P. Fantucci, R. Grandori, L. De Gioia, J. Mol. Graph. Model. 27 (2009) 889–899.
75. M. Amaral, D.B. Kokh, J. Bomke, A. Wegener, H.P. Buchstaller, H.M. Eggenweiler, P. Matias, C. Sirrenberg, R.C. Wade, M. Frech, Nat. Commun. 8 (2017) 2276.
76. J. Mieres-Perez, Y. Almeida-Hernandez, W. Sander, E. Sanchez-Garcia, Chem. Rev. 125 (2025) 7023–7056.
77. A.K. Bronowska, in: Thermodynamics-Interaction Studies-Solids, Liquids and Gases, IntechOpen, 2011.
78. E. Barratt, R.J. Bingham, D.J. Warner, C.A. Laughton, S.E. V Phillips, S.W. Homans, J. Am. Chem. Soc. 127 (2005) 11827–11834.
79. S. Wu, C. Liu, Y. Li, X. Zhang, Q. Han, H. Zhao, K. Zhao, Y. Dang, R. Wang, S. Song, Sci. Rep. 15 (2025) 24352.
80. A.D. Robertson, K.P. Murphy, Chem. Rev. 97 (1997) 1251–1268.